PHYSICAL REVIEW B **105**, 094410 (2022)

Editors' Suggestion

Magnetoelastic coupling anisotropy in the Kitaev material α-$RuCl_3$

Vilmos Kocsis,[1] David A. S. Kaib,[2] Kira Riedl,[2] Sebastian Gass,[1] Paula Lampen-Kelley,[3,4] David G. Mandrus,[3,4] Stephen E. Nagler,[5] Nicolás Pérez,[6] Kornelius Nielsch,[6] Bernd Büchner,[1,7] Anja U. B. Wolter,[1] and Roser Valentí[2]

[1] *Institut für Festkörperforschung, Leibniz IFW-Dresden, 01069 Dresden, Germany*
[2] *Institut für Theoretische Physik, Goethe-Universität Frankfurt, Max-von-Laue-Strasse 1, 60438 Frankfurt am Main, Germany*
[3] *Department of Materials Science and Engineering, University of Tennessee, Knoxville, Tennessee 37996, USA*
[4] *Materials Science and Technology Division, Oak Ridge National Laboratory, Oak Ridge, Tennessee 37831, USA*
[5] *Neutron Scattering Division, Oak Ridge National Laboratory, Oak Ridge, Tennessee 37831, USA*
[6] *Institut für Metallische Werkstoffe, Leibniz IFW-Dresden, 01069 Dresden, Germany*
[7] *Institut für Festkörper- und Materialphysik and Würzburg-Dresden Cluster of Excellence ct.qmat,*
Technische Universität Dresden, 01062 Dresden, Germany

(Received 8 September 2021; revised 1 January 2022; accepted 10 February 2022; published 7 March 2022)

The Kitaev material α-$RuCl_3$ is among the most prominent candidates to host a quantum spin-liquid state endowed with fractionalized excitations. Recent experimental and theoretical investigations have separately revealed the importance of both the magnetoelastic coupling and the magnetic anisotropy in dependence of the applied magnetic-field direction. In this combined theoretical and experimental research, we investigate the anisotropic magnetic and magnetoelastic properties for magnetic fields applied along the main crystallographic axes as well as for fields canted out of the honeycomb plane. We found that the magnetostriction anisotropy is unusually large compared to the anisotropy of the magnetization, which is related to the strong magnetoelastic $\widetilde{\Gamma}'$-type coupling in our *ab-initio* derived model. We observed large, nonsymmetric magnetic anisotropy for magnetic fields canted out of the honeycomb *ab* plane in opposite directions, namely, toward the $+c^*$ or $-c^*$ axes, respectively. The observed directional anisotropy is explained by considering the relative orientation of the magnetic field with respect to the coaligned $RuCl_6$ octahedra. Magnetostriction measurements in canted fields support this nonsymmetric magnetic anisotropy; however, these experiments are affected by magnetic torque effects. Comparison of theoretical predictions with experimental findings allow us to recognize the significant contribution of torque effects in experimental setups where α-$RuCl_3$ is placed in canted magnetic fields.

DOI: 10.1103/PhysRevB.105.094410

I. INTRODUCTION

Materials hosting quantum spin-liquid states have attracted much interest recently [1–7], as in these systems the quantum information may be protected from decoherence, and they can be applied in quantum computing technology [8]. A prime example for a theoretical model to host a quantum spin-liquid state is provided by the exactly solvable Kitaev model on the honeycomb lattice [9], which contains frustrated, bond-dependent magnetic interactions that lead to fractionalized quasiparticles, gauge fluxes and Majorana fermions. The investigation and experimental verification of quantum spin-liquid states presents, however, an ongoing challenge that has brought α-$RuCl_3$ to the forefront of research as a prime candidate for Kitaev physics.

While the honeycomb-layered α-$RuCl_3$ orders antiferromagnetically at low temperatures [10,11], the possibility of residual physics of fractionalization [12–16] or even a field-induced Kitaev spin-liquid state [17–19] have been intensively discussed. So far, numerous experimental methods have been used for the investigation of α-$RuCl_3$, including neutron and Raman scattering [13,19–24], specific heat [25], Grüneisen parameter [26], microwave and terahertz absorption [18,27,28], as well as thermal transport measurements [29–32] and notably some reporting a half-integer-quantized thermal Hall conductivity [33–36].

Various Raman scattering studies have reported pronounced Fano line shapes [20,22,23,37], which evidence a significant magnetoelastic coupling between the phonon modes and the magnetic continuum. Indeed, more recent thermal expansion and magnetostriction measurements have probed direct consequences of such coupling in α-$RuCl_3$ [38–40]. Strong magnetostrictive effects are plausible, considering those two aspects. First, magnetoelastic coupling is expected to be especially sensitive in Kitaev materials due to the strongly geometry-dependent exchange mechanisms [4,41,42]. Second, the weak van der Waals force between the honeycomb layers leads to large changes in the lattice parameters when mechanical stress is applied. We note that magnetoelastic coupling is necessarily in play when measuring a hypothetical spinful chiral edge current (that would be present in the Kitaev spin-liquid) [43,44]. Furthermore, magnetoelastic coupling could also lend the phonons themselves a bulk transverse (Hall) current, see, e.g., Ref. [45].

Further understanding of the intrinsic anisotropy in α-$RuCl_3$ could be gained by field-angular-dependent measurements. So far, significant magnetic torque effects have been found and investigated for various directions of the

©2022 American Physical Society

magnetic (H) field [46–49]. Additionally, specific heat and thermal conductivity measurements have been performed in magnetic fields applied in various in-plane and out-of-plane angles and revealed anisotropic thermodynamic and transport properties [32–36,50]. Therefore combined investigations of the magnetoelastic coupling and the magnetic anisotropy, using canted fields (i.e., fields tilted out of the honeycomb plane), can help to unveil the complex behavior of α-RuCl$_3$.

In this combined experimental and theoretical study, we focus on the angular, temperature, and magnetic-field dependence of the magnetic and magnetoelastic properties of α-RuCl$_3$. Depending on the in-plane field angle, we resolve a phase transition between different antiferromagnetic orders in accord with recent previous studies. In the presence of canted magnetic fields, we observe an anomalous increase in the magnetostriction at high fields related to the magnetic torque effects. The combination of magnetic measurements reveals a significant, nonsymmetric anisotropy for magnetic fields canted out of the hexagonal *ab* plane in opposite directions, upward or downward, namely, toward the $+c^*$ or $-c^*$ axes. This angular-anisotropy is related to the coaligned, corner-sharing RuCl$_6$ octahedra within the hexagonal planes. The experimentally observed magnetic and magnetoelastic anisotropy is the largest when the H field is rotated within the ac^* plane and smallest when rotated within the bc^* plane. To model the magnetostriction and the effect of magnetic torque, we employ *ab-initio*-derived magnetoelastic couplings [51], allowing us to separate the different contributions of the magnetoelastic interactions. The theoretical model provides a good qualitative description of the experimental observations, namely, predicting nonsymmetric angular-anisotropy for the ac^* plane while excluding it for the bc^* plane. However, our experiments and the theoretical model also point out the significant role of magnetic torque in those experiments, where the sample can freely move or deform, such as in magnetostriction and thermal transport measurements. In the case of magnetostriction measurement, the movement or deformation of the sample is on the sub-μm scale, while in the case of thermal transport measurements, the deformation can be significantly higher.

II. EXPERIMENTAL AND THEORETICAL METHODS

A. Experimental details

Single crystals of α-RuCl$_3$ were grown using the chemical vapor transport method [52]. The orientations of the monoclinic a and b axes with respect to the honeycomb plane were determined by angular-dependent magnetization measurements with $\mathbf{H} \in ab$ fields. The angular-dependent magnetization measurements were carried out in a SQUID magnetometer (MPMS-XL, Quantum Design). The field-dependent magnetization measurements up to $\mu_0 H = 14$ T were measured in a vibrating sample magnetometer (VSM, PPMS, Quantum Design). The precise 45 deg canting orientation of the crystals was ensured by a pair of appropriately cut quartz pads, between which the sample was fixed with varnish. The *ab*-plane orientation of the crystals was aligned under a microscope with ±1–2 deg angular precision.

The magnetostriction was measured using a custom-built dilatometer based on the capacitance measurement technique

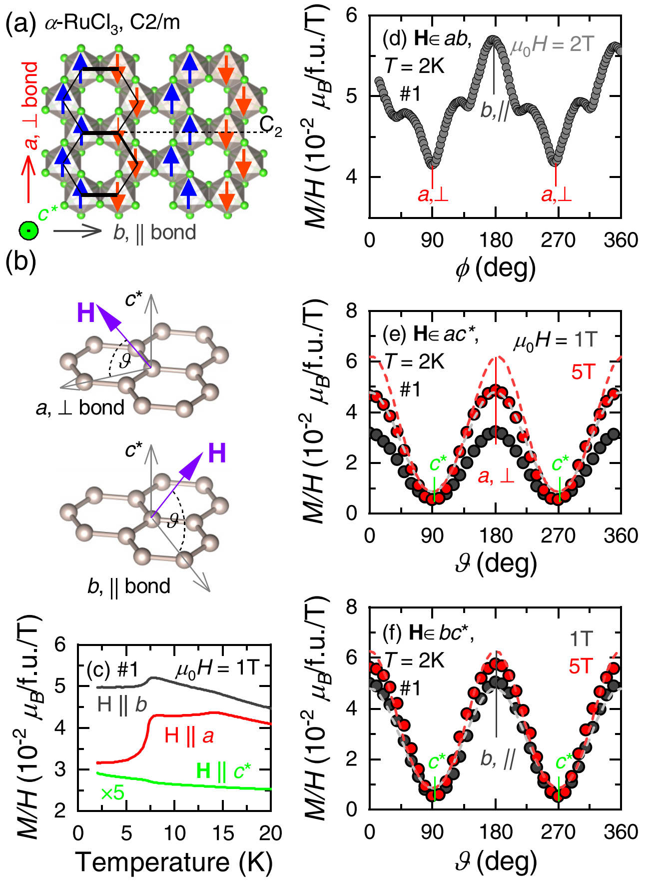

FIG. 1. (a) Single honeycomb layer of α-RuCl$_3$ and the crystallographic axes (a, b, and c^*). We highlight two directions within the *ab* plane; the a axis is perpendicular (⊥ *bond*) and the b axis is parallel (∥ *bond*) to one of the Ru-Ru bonds, respectively. Red and blue arrows at the honeycomb sites indicate the zigzag domain with ordering wave-vector $\mathbf{Q} \parallel b$. The dashed line indicates a C$_2$ rotation symmetry around an axis parallel to the b axis. (b) During the magnetization and magnetostriction measurements, the magnetic-field ($\mathbf{H}$) was canted out of the *ab* plane by an angle of ϑ, while the planar projection of the applied field was either along the a or b axis. (c) Temperature dependence of the magnetization for fields along the main crystallographic axes in the field cooling runs ($\mu_0 H = 1$ T). Note, that the data for $\mathbf{H} \parallel c^*$ are multiplied by a factor of 5 for better visibility. (d, e) Angular dependence of the magnetization at $T = 2$ K for fields rotated within the *ab*, ac^*, and bc^* planes, respectively. Measurement data are plotted with symbols (full circles) for $\mu_0 H = 1$ T and 5 T. In case of $\mathbf{H} \in ab$, the measurements are plotted for $\mu_0 H = 2$ T. Dashed curves in panels (e) and (f) correspond to the theoretical calculations.

(AH2700A, Andeen-Hagerling) [53]. Due to the dimensions of the available single crystals, the length change ΔL of the sample was measured along the c^* axis [$\Delta L_{c^*} \parallel c^*$; see Fig. 1(a)], while the H field could be applied in arbitrary directions via the rotation of the capacitance cell body or the sample. In this measurement technique, the sample is held in place in the dilatometer by a small uniaxial pressure applied on the sample during the mounting. Therefore if sufficient torque is applied, the sample may slightly rotate or deform within the dilatometer, which is measured as an apparent length change. This issue will be discussed in details in Sec. III as well as we give an estimate to its magnitude. During the magnetostriction measurement the magnetic field was swept between ±14 T with 0.01 T/min or 0.03 T/min rates at constant temperatures. The linear magnetostriction coefficient along the c^* axis (λ_{c^*}) was calculated as the H-field derivative of the relative length change:

$$\lambda_{c^*} = \frac{\partial}{\partial(\mu_0 H)}\frac{\Delta L_{c^*}(T,\mu_0 H)}{L_{c^*}(300\,K, 0\,T)}. \quad (1)$$

The measurements were performed on two different pieces of α-RuCl$_3$ crystals from the same batch (samples #1 and #2) with thicknesses of ~800 μm.

B. Theoretical details

We compare our measurements to numerical results on the extended Kitaev models. In such models, the bonds are labeled as X, Y, or Z depending on their orientation. For a nearest-neighbor Z-bond [parallel to the b axis; see Fig. 1(a)] with local C_{2h} symmetry, the symmetry-allowed magnetic exchange between the $J_{\rm eff} = \frac{1}{2}$ pseudospins, labeled as $\mathbf{S}_i$ and $\mathbf{S}_j$, is [54]

$$H_{\rm Z} = K S_i^z S_j^z + J\mathbf{S}_i\cdot\mathbf{S}_j + \Gamma\left(S_i^x S_j^y + S_i^y S_j^x\right) + \Gamma'\left(S_i^x S_j^z + S_i^z S_j^x + S_i^y S_j^z + S_i^z S_j^y\right), \quad (2)$$

where K and J correspond to the Kitaev and Heisenberg exchanges, respectively, while Γ, Γ' are symmetric off-diagonal exchanges. The X and Y bond exchanges can be constructed via the cyclic permutation of (x, y, z) in Eq. (2). The magnetic Hamiltonian is then given as the sum of these exchange terms (including possible longer-range terms) and the Zeeman term $H_{\rm Zee} = -\mu_B\mu_0\sum_i \mathbf{H}\cdot\mathbb{G}\cdot\mathbf{S}_i$, where $\mathbb{G}$ is the gyromagnetic tensor. To solve it, we employ exact diagonalization (ED) on a hexagon-shaped 24-site cluster. As a magnetic model, we discuss the *ab-initio* guided minimal model of Ref. [55], which has been shown to reproduce many experimental observations in α-RuCl$_3$ [22,25,26,49,55–58]. Here the exchange parameters are

$$(K,\ J,\ \Gamma,\ \Gamma',\ J_3) = (-5,\ -0.5,\ 2.5,\ 0,\ 0.5)\,{\rm meV}, \quad (3)$$

where J_3 denotes an additional third-nearest-neighbor Heisenberg exchange, and the components of $\mathbb{G}$ are $g_{ab} = 2.3$ and $g_{c^*} = 1.3$ for the in-plane and out-of-plane elements, respectively. Note that this model is C_3 simplified, i.e., the coupling magnitudes are equal on X, Y, and Z bonds. The $C2/m$ structure of α-RuCl$_3$ [10] does, however, slightly break C_3 symmetry, a property that manifests in the *in-plane* angle-dependent measurements discussed below and therefore it is not described in the present model by construction.

To model the spin-lattice coupling, we employ the *ab-initio*-derived linear magnetoelastic couplings of Ref. [51] for α-RuCl$_3$, defined as $\widetilde{\mathcal{J}} = (\frac{\partial\mathcal{J}}{\partial\epsilon})|_{\epsilon=0}$, where $\epsilon = \Delta L_{c^*}/L_{c^*}$ and $\mathcal{J}\in\{K, J, \dots, g_{ab}, g_{c^*}\}$. The strongest magnetoelastic exchange couplings are then

$$(\widetilde{K}, \widetilde{J}, \widetilde{\Gamma}, \widetilde{\Gamma'}) = (40.5,\ 1.3,\ 7.5,\ -11.5)\,{\rm meV} \quad (4)$$

and the magnetoelastic g couplings $(\widetilde{g_{ab}}, \widetilde{g_{c^*}}) = (-1.6,\ 3.85)$. Note that the predicted large magnetoelastic $\widetilde{\Gamma'}$ coupling in this model is a somewhat unexpected property, as the *magnetic* Γ' coupling is generally found to be subdominant or negligible in magnetic models of α-RuCl$_3$ (see, e.g., Ref. [59]). Nevertheless we find this large $\widetilde{\Gamma'}$ to be essential to reproduce the strong anisotropy found in our magnetostriction measurements, as discussed below. In our calculations we also include the weaker longer-range magnetoelastic couplings of Ref. [51], which, however, do not qualitatively change the results. For the magnetostriction, we then employ the approximation [51]

$$\lambda_{c^*} \approx \frac{\kappa_{c^*}}{V}\sum_{\mathcal{J}\in\{K,J,\dots\}}\widetilde{\mathcal{J}}\left(\frac{\partial M}{\partial\mathcal{J}}\right)_{\epsilon=0}, \quad (5)$$

where the sum goes through all strain-dependent interactions and g values. The parameter $\kappa_{c^*} \equiv -(\partial\epsilon/\partial p_{c^*})$ is the (unknown) linear compressibility along c^* against uniaxial pressure p_{c^*}. The field dependence of λ_{c^*} enters through the field dependencies of the magnetization susceptibilities $(\frac{\partial M}{\partial\mathcal{J}})_{\epsilon=0}$, which we compute using ED in the magnetic model described above.

III. MAGNETIC AND ELASTIC PROPERTIES IN CANTED MAGNETIC FIELDS

Each layer of α-RuCl$_3$ consists of edge-sharing RuCl$_6$ octahedra that form a honeycomb network, as shown in Fig. 1(a). For the crystal structure, both the rhomboedral $R\bar{3}$ [60–62] and the monoclinic $C2/m$ [10,63] structures are presently discussed in the literature. We employ the axis convention of the $C2/m$ structure, where the honeycomb plane is spanned by the crystallographic a and b axes, while c^* is perpendicular to it; see Fig. 1(a) and 1(b). Note that the b axis is parallel to one of the honeycomb bonds, while the a axis is perpendicular to the same bond.

The antiferromagnetic “zigzag” long-range order [10] [Fig. 1(a)] develops at $T_{\rm N} = 7.1$ K, as shown by the magnetization data [Fig. 1(c)] in moderate $\mu_0 H = 1$ T fields applied along the main crystallographic axes. The magnetization curves for $\mathbf{H}\parallel a$ and $\mathbf{H}\parallel b$ show a sudden decrease at $T_{\rm N}$; however, the weaker temperature dependence for $\mathbf{H}\parallel b$ suggests that the ordered moments are perpendicular to the b axis. The particular zigzag domain structure associated to such ordering [64], where the ordered moments lie in the ac^* plane, is illustrated in Fig. 1(a). Note that the minor transition apparent for $\mathbf{H}\parallel a$ at $T = 14$ K is indicative of the so-called ABC/ABAB-stacking faults [11,65].

For fields applied perpendicular to the honeycomb plane ($\mathbf{H}\parallel c^*$), a much smaller susceptibility is found, highlighting the strong easy-plane anisotropy in α-RuCl$_3$. This is further resolved in Figs. 1(e) and 1(f), where the field is rotated within the ac^* plane or bc^* plane, respectively [cf. Fig. 1(b)], in the presence of constant field strength and temperature $T = 2$ K. Corresponding theoretical $T = 0$ K results within the magnetic minimal model (see Section II B) agree well with the measurement; see dashed lines in Figs. 1(e) and 1(f). In case of magnetic properties, the easy-plane anisotropy is primarily facilitated by the strong Γ term and the anisotropic g tensor [49,66]. Note that theoretical curves in Figs. 1(e) and 1(f) are identical, while the experimental curves are different for $\mathbf{H} \in ac^*$ and $\mathbf{H} \in bc^*$. This is explained by our C_3-symmetrized model, which suppresses the *in-plane* anisotropy, whereas the real α-RuCl$_3$ is apparently monoclinic. Therefore the agreement between theory and experiment is excellent only in Fig. 1(f). Nevertheless, we obtain overall semiquantitative agreement between theory and experiment.

Figure 1(d) shows the field-angular dependence of the magnetization within the *ab* honeycomb plane for moderate $\mu_0 H = 2$ T. In the angular dependence, components with clear twofold and sixfold symmetries are identified. Assuming a honeycomb lattice with C_6 symmetry, as present in the proposed $R\bar{3}$ structure of α-RuCl$_3$, only an angular dependence with sixfold symmetry is expected. A spontaneous selection of single-domain zigzag magnetic order can break the sixfold symmetry and give a component with twofold symmetry. However, the same angular dependence of M as shown in Fig. 1(d) is reproduced repeatedly for every measurement, even after heating the sample to room temperature, well above T_N. Hence the preference of zigzag domain selection with respect to the crystallographic axes is consistent and probably related to the crystal structure, compatible with the suggested monoclinic C2/m space group. Accordingly, the zero-field magnetic Hamiltonian favors certain zigzag domains energetically out of the three possible domain directions. From the measured angular preference we infer, analogously as done in Ref. [67], that in our sample the dominant domain at low field is that with ordering wave-vector $\mathbf{Q} \parallel b$ [as illustrated in Fig. 1(a)]. While this domain is expected to stay stable at finite fields $\mathbf{H} \parallel b$, a reorientation to the other zigzag domains is expected at an intermediate field when $\mathbf{H} \parallel a$ [56,67].

Figure 2 shows the experimental c^*-axis magnetostriction [λ_{c^*}, Eq. (1)] as a function of magnetic-field $\mathbf{H} \parallel a$ for selected temperatures within the ordered temperature regime, the short-range correlated Kitaev paramagnet, and the conventional thermal paramagnet. The magnetostrictions measured in increasing and decreasing fields were found to be identical within the accuracy of the measurement. At $T = 3$ K, the magnetostriction λ_{c^*} has a positive peak at low fields and a sharp negative double-peak structure at higher fields. The positive peak at $\mu_0 H_0 = 0.7$ T corresponds to the aforementioned domain repopulation of the antiferromagnetic order and it is present in both the field-increasing and the -decreasing runs. We resolve two sharp negative peaks at $\mu_0 H_1 = 6.4$ T and $\mu_0 H_2 = 7.2$ T. The former is a phase transition at $\mu_0 H_1$ where the interplane ordering between the zigzag-ordered honeycomb planes changes [68], while the latter at $\mu_0 H_2$ is the transition where the zigzag magnetic order disappears. In agreement with Refs. [58,67,68], the extent between these two phases is the largest for $\mathbf{H} \parallel a$ and the smallest or absent for $\mathbf{H} \parallel b$ [cf. Fig. 3(a)]. At $T = 5$ K, the double-peak structure merges into a single, negative peak at $\mu_0 H_1 = 6.3$ T. Above $T_N = 7.1$ K, the sharp peaks of the low-temperature magnetostriction are replaced by broad field-dependent features. For $T \gtrsim 30$ K, the magnetostriction shows a linear field dependence, as expected for a conventional thermal paramagnet [69]. In contrast, for intermediate temperatures $T_N < T \lesssim 30$ K, we find the magnetostriction to show a nonlinear and nonmonotonic field dependence. This appears to be a property of the short-range correlated Kitaev paramagnet [13,14,56,70] in this temperature range.

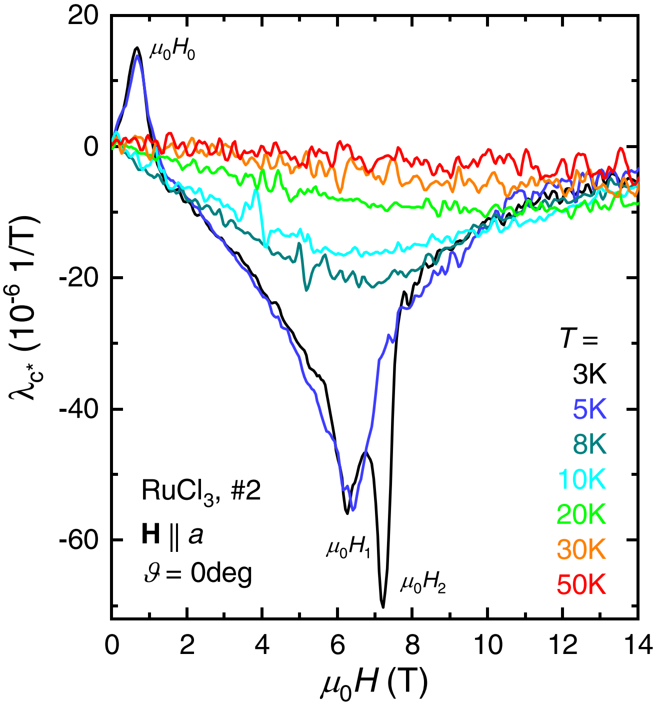

FIG. 2. Magnetic-field dependence of the λ_{c^*} linear magnetostriction coefficient at selected temperatures. The ΔL length change was measured along the c^* axis and $\mathbf{H} \parallel a$ magnetic field was applied, perpendicular to one of the Ru-Ru bonds.

The λ_{c^*} magnetostriction with fields applied along the main crystallographic axes as well as for $\mathbf{H}$ canted out from the *ab* plane is shown in Fig. 3(a). The experimental configuration and the definition of the ϑ canting angle is illustrated in Fig. 3(c); the H field is canted away from the a axis by angle ϑ within the ac^* plane. The measurement with $\vartheta = 0$ deg and 90 deg corresponds to $\mathbf{H} \parallel a$ and $\mathbf{H} \parallel c^*$, respectively. For better comparison and for the sake of completeness, we present the $\mathbf{H} \parallel b$ data reproduced after Ref. [39] [dashed pink line in Fig. 3(a)]. The λ_{c^*} magnetostriction for $\mathbf{H} \parallel b$ has one single negative peak at $\mu_0 H = 7.5$ T. Unlike λ_{c^*} for $\mathbf{H} \parallel a$, no significant domain reorientation at low fields is visible, as expected for the identified dominant $\mathbf{Q} \parallel b$ zigzag domain [Fig. 1(a)]. In contrast to the in-plane field results, the magnetostriction for $\mathbf{H} \parallel c^*$ is small and shows weak, nonmonotonous field dependence. The $\mu_0 H_1$ and $\mu_0 H_2$ critical fields of the two peaks in the magnetostriction data approximately follow a simple $\sim 1/\cos\vartheta$ angular dependence, as shown in Fig. 3(b). Such an angular dependence is expected if the phase transitions are entirely driven by the in-plane component of the magnetic field. We note that the $\mu_0 H_0$ critical field does not follow the $\sim 1/\cos\vartheta$ angular dependence. This deviation suggests that the reorientation of the three differently oriented zigzag domains in the presence of canted fields has a nontrivial energetic competition.

Theoretical calculations for the $\lambda_{c^*}/\kappa_{c^*}$ magnetostriction are shown in Fig. 3(c) for the same field configurations as in Fig. 3(a). The calculated magnetostrictions for fields applied

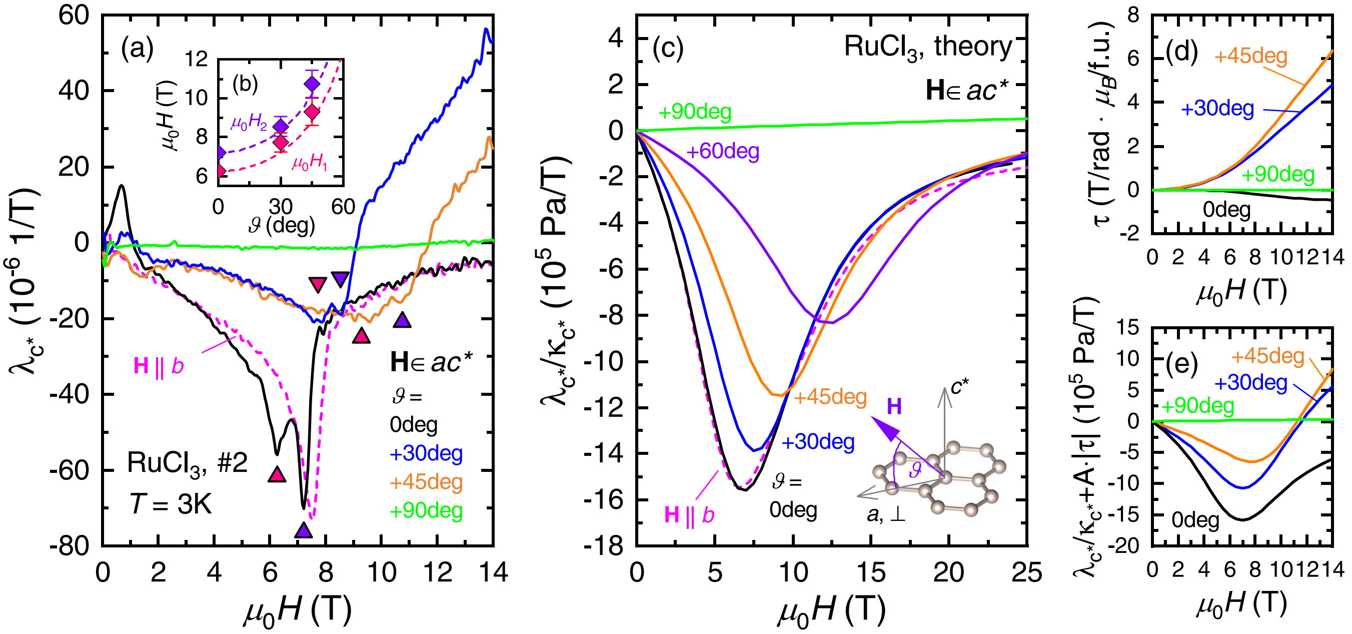

FIG. 3. (a) Field dependence of the linear magnetostriction coefficient λ_{c^*} at $T = 3$ K. The magnetic field was applied along the main crystallographic axes, as well as canted out of the *ab* plane with projection perpendicular to the bond ($\mathbf{H} \in ac^*$). The $\vartheta = 0$ deg and 90 deg angles correspond to the *a* and c^* axes, respectively. The two peaks in the λ_{c^*} data correspond to ($\mu_0 H_1$) a phase transition between different zigzag interplane orderings and ($\mu_0 H_2$) a transition into the field-induced quantum paramagnetic phase. The $\mu_0 H_1$ and $\mu_0 H_2$ phase boundaries are indicated by triangles, respectively. (b) Angular dependence of the $\mu_0 H_1$ and $\mu_0 H_2$ phase-transition fields. The dashed lines indicate the $\sim 1/\cos\vartheta$ field dependence. (c) The field dependence of the $\lambda_{c^*}/\kappa_{c^*}$ magnetostriction calculated for H field canted out of the *ab* plane with ϑ angle, $\mathbf{H} \in ac^*$. The inset defines the field angle ϑ. Note that panels (a) and (c) are shown for different field scales. (d) Magnetic-field dependence of the calculated τ magnetic torque for selected ϑ canting angles, $\mathbf{H} \in ac^*$. (e) The effect of magnetic torque on the field dependence of the magnetostriction is modeled with the $\lambda_{c^*}/\kappa_{c^*} + A \cdot |\tau|$ relation with the same $A = 2.2 \cdot 10^5$ Pa · Rad / ($\mathrm{T}^2 \cdot \mu_B$/f.u.) parameter fitted for each curve.

along the main crystallographic axes (a, b, c^*) qualitatively reproduce the measured data. In the experiments, we ascribed the measured $\mu_0 H_0 = 0.7$ T peak to the zigzag domain reorientation. However, in our C_3-symmetrized model, there is no preferred domain orientation at $\mu_0 H = 0$ T and therefore no reorientation is expected. Moreover, due to the restriction to a two-dimensional finite cluster in the calculations, the results are limited in the reproduction of the lower-field peak $\mu_0 H_1$ for $\mathbf{H} \parallel a$ (related to the interlayer reordering [68]), and peaks at phase transitions are generally expected to be broadened. When the magnetic field is tilted out of the *ab* plane, $\mathbf{H} \in ac^*$, theoretical calculations show that the peaks in the $\lambda_{c^*}/\kappa_{c^*}$ become smaller and appear at higher fields. While the experimental data in Fig. 3(a) for $\vartheta = 30$ deg and 45 deg retain the double-peak-like features in λ_{c^*}, they differ significantly from the calculations. In contrast to the theory, the measured λ_{c^*} magnetostriction for $\theta = 30$ deg and 45 deg changes sign at intermediate field strengths due to a large positive component added to the measurement.

We attribute the observed anomalous component to magnetic torque effects. When the magnetic torque is strong, it could rotate, bend, and deform the α-RuCl$_3$ crystal within the dilatometer, as discussed in Supplemental Fig. S2. Theoretical calculations for the magnetic torque $\tau = \frac{dF}{d\vartheta}$ (F being the free energy) for $\mathbf{H} \in ac^*$ are shown in Fig. 3(d). The torque, facilitated by Γ exchange and g anisotropy [49], is small for fields along the main crystallographic axes ($\vartheta = 0$ deg and $\vartheta = 90$ deg) but becomes large for intermediate canting angles where it strongly increases with field strength. Although the H field points along a main crystallographic axis for $\vartheta = 0$ deg, ($\mathbf{H} \parallel a$), a small but nonzero torque persists anyway. Note that no symmetry in the Hamiltonian requires the torque to be maximal at $\theta = 45$ deg. While the presently employed model parameters predict the magnetic torque to reach its maximum close to $\vartheta = 45$ deg in Fig. 3(d), a smaller g-tensor anisotropy can further decrease the canting angle needed for maximum torque. This can explain why the positive contribution in the λ_{c^*} magnetostriction measurement is larger for $\vartheta = 30$ deg than for $\vartheta = 45$ deg in Fig. 3(a). This further demonstrates that the effect of magnetic torque on the magnetostriction measurements is a complex issue, which depends on the spring constant, pressure setting, and dimensions of the dilatometer as well as the dimensions and elastic constants of the sample. For small rotations (deformations), it is reasonable to assume that the change in the magnetostriction is linear in the torque as $\Delta\lambda_{c^*}/\kappa_{c^*} \sim A \cdot |\tau|$, where A is a material, measurement setup, and pressure setting dependent, but field magnitude- and angle-independent constant. Figure 3(e) illustrates the modified magnetostriction calculated with the $\lambda_{c^*}/\kappa_{c^*} + A \cdot |\tau|$ relation, where $A = 2.2 \cdot 10^5$ Pa · Rad / ($\mathrm{T}^2 \cdot \mu_B$/f.u.) is a fixed value for all curves. The A parameter was fitted to the $\vartheta = 45$ deg data with the highest magnetic torque τ, so that $\lambda_{c^*}/\kappa_{c^*}(H^*) + A \cdot |\tau| = 0$ is satisfied for the theoretical data at the same H^* field as the measured magnetostriction ($\lambda_{c^*}(H^*) = 0$). This qualitatively models that the strong positive contributions to λ_{c^*} in the

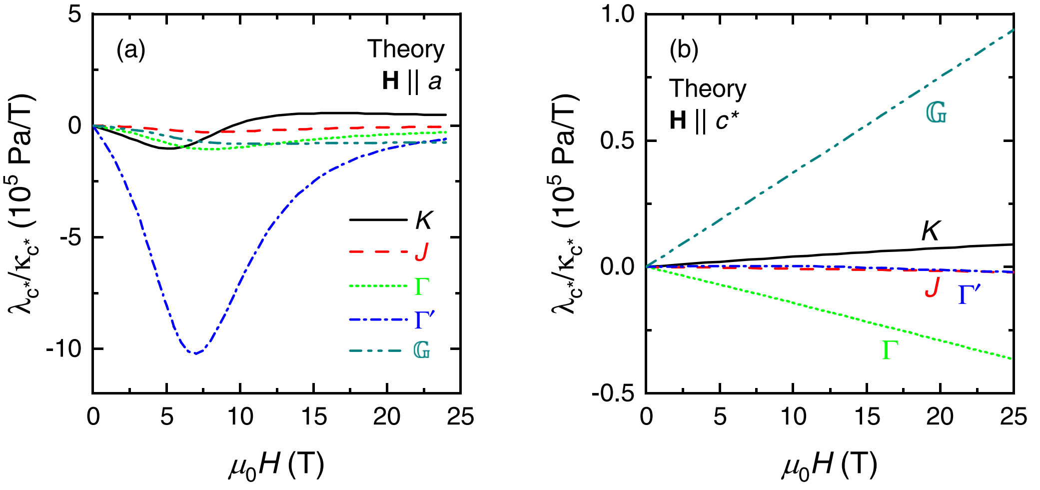

FIG. 4. Dissection of the largest contributions to theoretical magnetostriction through Eq. (5). Each curve corresponds to a component of Eq. (5) with different $\mathcal{J}$. The notation K, J, Γ, Γ', and $\mathbb{G}$ corresponds to the summand components of $\frac{1}{V}\widetilde{K}(\frac{\partial M}{\partial K})$, $\frac{1}{V}\widetilde{J}(\frac{\partial M}{\partial J})$, $\frac{1}{V}\widetilde{\Gamma}(\frac{\partial M}{\partial \Gamma})$, $\frac{1}{V}\widetilde{\Gamma}'(\frac{\partial M}{\partial \Gamma'})$, and $\frac{1}{V}\widetilde{\mathbb{G}}(\frac{\partial M}{\partial \mathbb{G}})$, respectively. The line with $\mathcal{J} = \mathbb{G}$ corresponds to magnetoelastic coupling with the g tensor. (a) In-plane field $\mathbf{H} \parallel a$ ($\vartheta = 0$deg); (b) out-of-plane field $\mathbf{H} \parallel c^*$ ($\vartheta = 90$deg).

measurements with canted fields ($\vartheta = +30$ deg and $+45$ deg) are related to the rotational effect of the magnetic torque and not intrinsic to the sample. However, note that even with these efforts, the effect of torque cannot be removed from the measurement data in a quantitative manner.

Focusing back on the crystallographic axes a ($\vartheta = 0$ deg) and c^* ($\vartheta = 90$ deg), where torque effects are expected to be much weaker, we point out a much stronger anisotropy found in λ_{c^*} than expected from the magnetization anisotropy [69]. In principle, due to the Maxwell relation $\lambda_{c^*} = -\partial M/\partial p_{c^*}$, one can expect λ_{c^*} to be roughly proportional to the magnetization M at small field strengths. However, this does not explain the observed angular dependence of λ_{c^*}; while the magnetization for $\vartheta = 90$ deg is already reduced by a factor of $\sim$6 to 10 compared with $\vartheta = 0$ deg [cf. Fig. 1(e)], this alone cannot account for the much larger $\sim$30-fold reduction of the magnetostriction between $\vartheta = 90$ deg and $\vartheta = 0$ deg [cf. Fig. 3(a)]. This increased anisotropy effect is also reproduced in our model calculations [Fig. 3(c)]. In the calculations, we can trace the unusual reduction in magnetostriction back to contributions from different magnetoelastic couplings, i.e., from different summands in Eq. (5). The largest entering magnetoelastic couplings $\widetilde{\mathcal{J}}$ are the nearest-neighbor anisotropic couplings $\widetilde{K}, \widetilde{\Gamma}, \widetilde{\Gamma}'$, which are field independent. The field-strength and field-direction dependency enters through the susceptibilities $\partial M/\partial \mathcal{J}$. Figure 4(a) shows the largest summands ($\widetilde{\mathcal{J}} \cdot \partial M/\partial \mathcal{J}$) as a function of in-plane field $\mathbf{H} \parallel a$ ($\vartheta = 0$deg), where a dominating effect from the contribution with $\mathcal{J} = \Gamma'$ is demonstrated. The large susceptibility $\partial M/\partial \Gamma'$ for in-plane fields can be understood from the fact that Γ' is the exchange that tunes most strongly the easy-plane anisotropy of α-RuCl$_3$ [71]. However, for out-of-plane fields $\mathbf{H} \parallel c^*$, variations in Γ' have little effect onto the magnetization. Therefore the large $\widetilde{\Gamma}'$-contribution breaks off for $\mathbf{H} \parallel c^*$, leading to a much smaller λ_{c^*} as shown in Fig. 4(b). The agreement with experiment therefore confirms the presence of a strong *negative* magnetoelastic $\widetilde{\Gamma}'$ coupling in α-RuCl$_3$ [see Eq. (4)]. Note that the large $\widetilde{\Gamma}' < 0$ suggests that the application of 3 to 5% compressive uniaxial c^*-strain may destabilize the zigzag magnetic order [51]. While α-RuCl$_3$ in measurements under hydrostatic pressure show dimerization [72,73], the application of uniaxial strain leads to fundamentally different lattice deformations. As an example, compression along the c^*axis expands the lattice within the ab plane, in contrast with the application of hydrostatic pressure, which compresses both the c^*axis and the honeycomb ab plane. Another estimate for the uniaxial pressure dependence of T_{N} comes from the Ehrenfest relation [69]:

$$\frac{\partial T_{\mathrm{N}}}{\partial p_{c^*}} = V_{\mathrm{mol}} T_{\mathrm{N}} \frac{\Delta \alpha_{c^*}}{\Delta C_p}, \tag{6}$$

where p_{c^*} is the uniaxial pressure applied along the c^*axis, V_{mol} is the molar volume, and ΔC_p and $\Delta \alpha_{c^*}$ are the heights of the anomaly in the specific heat and thermal expansion at T_{N}, respectively. Using specific-heat data $\Delta C_p = 3.0$ J/mol/K from Ref. [25], $\Delta \alpha_{c^*} = -7 \cdot 10^{-5}$ 1/K from Ref. [39], and $V_{\mathrm{mol}} = 5.26 \cdot 10^{-5}$ m^3/mol, we get $\frac{\partial T_{\mathrm{N}}}{\partial p_{c^*}} \approx -8.8$ K/GPa. This means that a noticeable change in T_{N} can be obtained under experimentally achievable conditions [74]. While the magnetostriction measurements under canted magnetic fields are strongly affected by the magnetic torque, the magnetization measurements are unaffected, as the sample is strongly fixed to a rigid sample holder. Figure 5 reveals an interesting anisotropy found in the magnetization measurements for fields rotated out of the ab plane into opposite directions (i.e., toward $+c^*$ or $-c^*$). Magnetization measurements at $T = 2$ K for $\mathbf{H} \in ac^*$ and $\mathbf{H} \in bc^*$, canted out of the ab plane by $\vartheta = \pm 45$ deg angles, are shown in Figs. 5(a)–5(c) and 5(d)–5(f), respectively. Figures 5(a), 5(d), 5(b), 5(e), and 5(c), 5(f) show the H-field dependence of the magnetization, the field derivative, and the field dependence of the ΔM magnetization difference between the $\vartheta = +45$ deg and the -45 deg measurements ($\Delta M = M_{+45\,\mathrm{deg}} - M_{-45\,\mathrm{deg}}$), respectively. For $\mathbf{H} \in ac^*$, in Fig. 5(a), the field dependence of the magnetization for $\vartheta = +45$ deg and -45 deg shows clear differences above $\mu_0 H = 8$ T, while those of $\mathbf{H} \in bc^*$ show

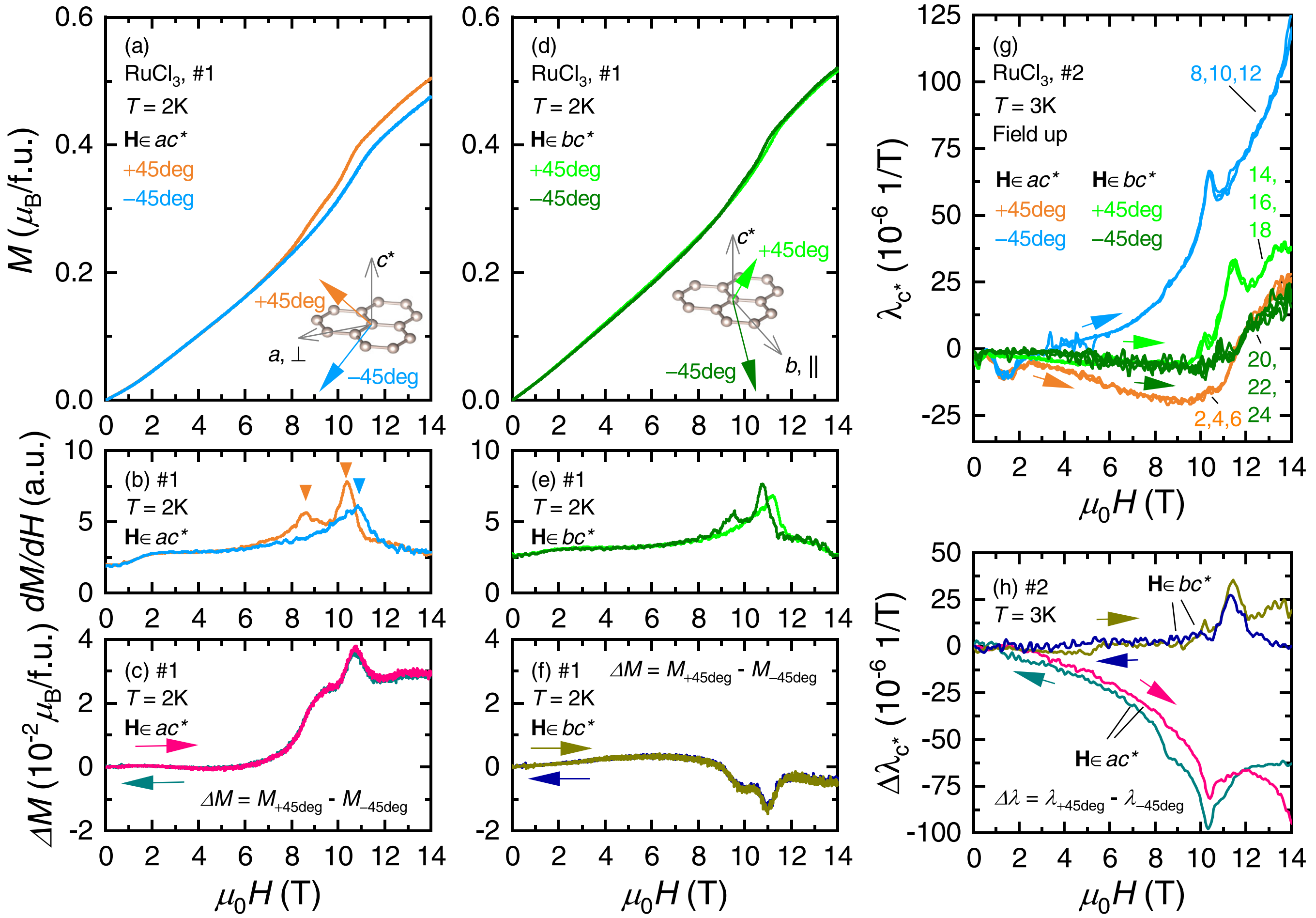

FIG. 5. (a) Magnetic-field dependence of the magnetization at $T = 2$ K for $\mathbf{H} \in ac^*$ with $\vartheta = \pm 45$ deg canting out of the ab plane. (b) Magnetic-field dependence of the field derivative and (c) the field dependence of the ΔM magnetization difference for the $\vartheta = +45$ deg and -45 deg measurements ($\Delta M = M_{+45\,\mathrm{deg}} - M_{-45\,\mathrm{deg}}$). The phase transitions for $\mathbf{H} \in ac^*$ are indicated by triangles as peaks in dM/dH. (d–f) Magnetic-field dependence of the magnetization, field derivative, and ΔM at $T = 2$ K for $\mathbf{H} \in bc^*$, $\vartheta = \pm 45$ deg. (g) Magnetic-field dependence of the λ_{c^*} magnetostriction coefficient at $T = 3$ K for $\mathbf{H} \in ac^*$ and $\mathbf{H} \in bc^*$ measured in the field-increasing runs with $\vartheta = \pm 45$ deg canting angles. Three λ_{c^*}-H curves are shown for each configuration with numerals indicating the order of the measurements (complete list is shown in the Supplemental Material [75], Fig. S1). The experimental conditions are illustrated as an inset in panels (a) and (d). While panels (a, b, d, e, and g) show measurements for the field-increasing runs, panels (c, f, and h) show the measurements for the field-increasing and -decreasing runs.

small differences only. Moreover, peaks in the field derivative of the magnetization [Fig. 5(b)] indicate two phase transitions for the $\vartheta = +45$ deg measurement at $\mu_0 H_1 = 8.6$ T and $\mu_0 H_2 = 10.3$ T, while in the $\vartheta = -45$ deg measurement there is only one peak seen at $\mu_0 H_2' = 10.9$ T. Note that the field derivatives in the $\mathbf{H} \in bc^*$ measurements are similar to those of the $\mathbf{H} \in ac^*$ experiments; however, here the $\vartheta = -45$ deg measurement has two peaks in dM/dH and the $\vartheta = +45$ deg measurement has one at slightly different fields. The ΔM magnetization difference in Fig. 5(c) shows a shoulder-like magnetization change starting from $\mu_0 H = 8.5$ T and a peak at around $\mu_0 H = 10.7$ T. The ΔM magnetization difference for $\mathbf{H} \in bc^*$ in Fig. 5(f) is about four times smaller and has the opposite sign than those for $\mathbf{H} \in ac^*$.

For comparison, Fig. 5(g) shows the field dependence of the λ_{c^*} magnetostrictions for $\mathbf{H} \in ac^*$ and $\mathbf{H} \in bc^*$ fields canted out from the ab plane in $\vartheta = \pm 45$ deg angles for the field-increasing runs. The complete set of measurements for the field-increasing and -decreasing runs are shown in Fig. S1, while additional measurements on sample #1 are shown in Fig. S3 [75]. During the λ_{c^*} - H measurements the H field was swept between ±14 T several times, then the sample was removed and rotated to the next measurement configuration. Curves labeled as field up and field down refer to measurements in H field with increasing or decreasing magnitudes, respectively. In Figs. 5(g), S1, S2, and S3 we show three λ_{c^*} - H curves to demonstrate the signal to noise level, while Fig. S3 discusses the reproducibility when we change the ϑ canting angle. Note that these magnetostriction measurements in such canted fields show significant hysteresis. However, the difference between the +45 deg and the −45 deg magnetostriction, $\Delta\lambda_{c^*} = \lambda_{c^*,+45\,\mathrm{deg}} - \lambda_{c^*,-45\,\mathrm{deg}}$ [Fig. 5(h)], is found to be rather independent of the direction of the field sweep. Similarly to the magnetization measurements, the magnetostriction shows a significant difference $\Delta\lambda_{c^*}$ for $\mathbf{H} \in ac^*$ but a small one for $\mathbf{H} \in bc^*$. Furthermore we can also

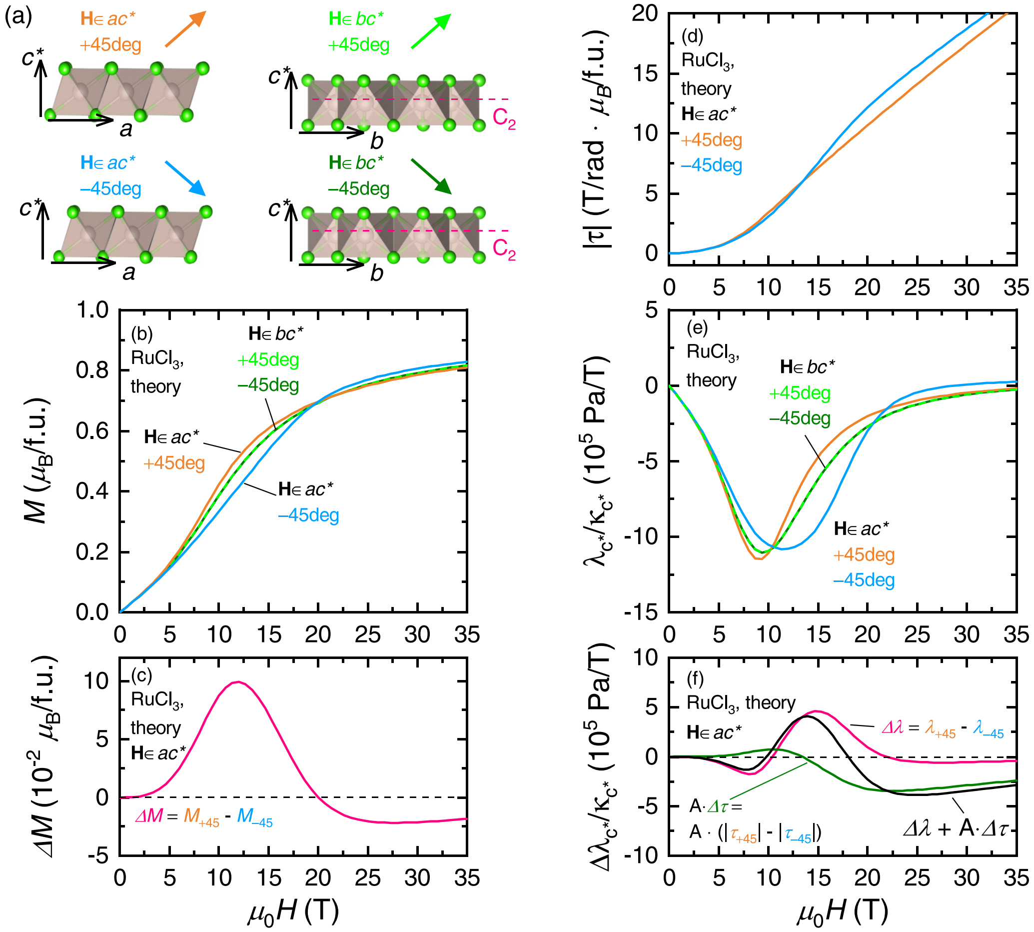

FIG. 6. (a) Schematic illustration of the measurement configurations for each experiment. For $\mathbf{H} \in ac^*$, $\vartheta = +45$ deg, and $\vartheta = -45$ deg, the net magnetization points along the vertexes and the edges of the Cl_6 octahedra, respectively. In both cases of $\mathbf{H} \in bc^*$, $\vartheta = \pm 45$ deg, the net magnetization points along the side of the RuCl_6 octahedra, which configurations are connected by the C_2 rotation in the honeycomb plane. (b) Magnetic-field dependence of the magnetization and (c) ΔM magnetization difference calculated for $\mathbf{H} \in ac^*$ and $\mathbf{H} \in bc^*$ with $\vartheta = \pm 45$ deg canting out of the *ab* plane. (d) magnetic-field dependence of the τ magnetic torque for $\mathbf{H} \in ac^*$, $\vartheta = \pm 45$ deg. (e) Magnetic-field dependence of $\lambda_{c^*}/\kappa_{c^*}$ magnetostriction and (f) $\Delta\lambda_{c^*}/\kappa_{c^*}$ magnetostriction difference, calculated for $\mathbf{H} \in ac^*$ and $\mathbf{H} \in bc^*$, $\vartheta = \pm 45$ deg. The effect of the magnetic torque on the $\Delta\lambda_{c^*}/\kappa_{c^*}$ magnetostriction difference is illustrated in panel (f); the torque is scaled to the unit of $\lambda_{c^*}/\kappa_{c^*}$ with $A = 2.2 \cdot 10^5$ Pa · Rad / ($\mathrm{T}^2 \cdot \mu_B$/f.u.).

observe a shoulder above $\mu_0 H = 8$ T and a peak at $\mu_0 H = 10.4$ T for $\mathbf{H} \in ac^*$. Note that the ΔM and $\Delta\lambda_{c^*}$ curves show a different field dependence at low fields, which is related to torque effects not compensated by the subtraction.

Theoretical calculations for the field dependence of the magnetization are shown in Fig. 6(b) with the experimental configurations illustrated in Fig. 6(a) for $\mathbf{H} \in ac^*$ as well as for $\mathbf{H} \in bc^*$ with fields canted out of the *ab* plane by $\vartheta = \pm 45$ deg. Note that the theoretical calculations are plotted on a wider field range than those of the measurements. In line with the experimental observations, the theoretical calculations confirm the different M-H curves between the $\vartheta = +45$ deg and the -45 deg canting angles for $\mathbf{H} \in ac^*$, and the calculated ΔM is shown in Fig. 6(c). This nonsymmetric difference in the magnetization is related to the orientation of the Ru^{3+} magnetic moment within the Cl_6 octahedra, schematically illustrated in Fig. 6(a). For $\vartheta = +45$ deg and -45 deg angles with $\mathbf{H} \in ac^*$, the net magnetization points roughly toward the top vertex or toward the midpoint of the edge of the RuCl_6 octahedra, respectively. For $\mathbf{H} \in bc^*$, the calculated M-H curves are exactly the same for the $\vartheta = +45$ deg and -45 deg cases. In these cases, the Ru^{3+} magnetic moments are pointing toward another edge of the RuCl_6 octahedra in sideways. Both cases are connected by the C_2 rotation symmetry around the *b* axis and therefore yield an identical response in an ideal crystal. The small ΔM difference observed for the $\mathbf{H} \in bc^*$ measurements can be related to twinning faults, where the honeycomb layers are rotated by 30 deg with respect to each other. This twinning fault is a different structural defect from the earlier recognized ABC/ABAB-stacking faults [11,65].

Calculations for the field dependence of the magnetic torque τ, magnetostriction $\lambda_{c^*}/\kappa_{c^*}$, and the magnetostriction difference $\Delta\lambda_{c^*}/\kappa_{c^*}$ for $\mathbf{H} \in ac^*$ and $\vartheta = \pm 45$ deg canting angles are shown in Figs. 6(d), 6(e), and 6(f), respectively. Similarly to the experimental observations, the field dependence of $\lambda_{c^*}/\kappa_{c^*}$ is different for $\vartheta = +45$ deg and -45 deg, and $\Delta\lambda_{c^*}/\kappa_{c^*}$ is finite for $\mathbf{H} \in ac^*$. For $\mathbf{H} \in bc^*$ and $\vartheta = \pm 45$ deg, the $\lambda_{c^*}/\kappa_{c^*}$ curves are identical, similarly to the magnetization. In order to account for the effect of the magnetic torque on the experimental data, Figure 6(d) shows calculations for the τ magnetic torque for $\mathbf{H} \in ac^*$, $\vartheta = \pm 45$ deg. While the magnetic torque for both $\vartheta = \pm 45$ deg is large, the calculations show only slight differences in the magnitudes of the magnetic torques, i.e., the $A \cdot \Delta\tau = A \cdot |\tau_{+45\,\text{deg}} - \tau_{-45\,\text{deg}}|$ is relatively small. Still, we find that the modeled $A \cdot \Delta\tau$ is comparable in magnitude to $\Delta\lambda_{c^*}/\kappa_{c^*}$, which is shown in Fig. 6(f) with the same scaling factor as in Fig. 3(e) for $\vartheta = +45$ deg. This means that it is not possible to subtract the effect of torque on the measurements by simply measuring and subtracting the magnetostrictions in the $\pm\vartheta$ configurations. Therefore we consider the experimentally observed $\Delta\lambda_{c^*}$ in Fig. 5(h) as an aggregate of the real $\vartheta = \pm 45$ deg nonsymmetric anisotropies in the magnetostriction and a finite magnetic torque. Additional theoretical calculations for the angular dependence of the magnetization for $\mathbf{H} \in ac^*$ and $\mathbf{H} \in bc^*$ are shown in Fig. S4 [75].

IV. SUMMARY

We have studied the magnetic anisotropy in the Kitaev-candidate material α-RuCl$_3$ using field-dependent magnetization and magnetostriction λ_{c^*} measurements. During these measurements, the magnetic field was selectively applied both along the main crystallographic axes or canted out from the honeycomb plane, while the length changes in the λ_{c^*} experiments were always measured along the c^* axis. The field dependence of the low-temperature λ_{c^*}-H magnetostriction measurements shows a double-peak structure for $\mathbf{H} \parallel a$ (perpendicular to one of the Ru-Ru bonds) and a single peak for $\mathbf{H} \parallel b$ (parallel to that Ru-Ru bond). This is in agreement with the extent of the recently reported intermediate ordered phase with modified interplane ordering [58,68].

We found that the λ_{c^*}-H measurements show an unusually increased degree of field-angular anisotropy compared with the magnetization measurements ($\mathbf{H} \parallel a$ and $\mathbf{H} \parallel b$ experiments compared with $\mathbf{H} \parallel c^*$). This suggests an additional degree of anisotropy in the magnetoelastic couplings. Our theoretical calculations based on *ab-initio* derived magnetoelastic couplings show that this effect can be explained through the presence of a strong magnetoelastic $\widetilde{\Gamma}'$-type coupling. The presence of the latter implies the possibility to destabilize the magnetic order via the application of uniaxial compressive strain.

Both the M-H and the λ_{c^*}-H measurements in the presence of canted fields show large differences and demonstrate a significant angular asymmetry when fields are canted away from the a axis toward $+c^*$ or $-c^*$ axes ($\mathbf{H} \in ac^*$), i.e., for positive or negative canting angles of the H field. This angular asymmetry stems from the orientation of the $\mathbf{H}$ field with respect to the coaligned RuCl$_6$ octahedra. However, we found that the magnetic torque has a strong influence on our magnetostriction measurements. From theory, magnetic torque is expected to be large only for canted field directions. We confirmed that the magnetic torque can qualitatively account for the measured field dependence of the magnetostriction and can contribute to the difference between the magnetostrictions measured in positive and negative ϑ canting angles. This implies that when performing or comparing experiments in canted magnetic fields where the samples of different sizes are free standing, such as in the case of dilatometry or thermal Hall measurements, due to the very soft mechanical properties of α-RuCl$_3$ the magnetic torque may add relevant contributions to the measurements via plastic distortion or tilting of the crystals.

ACKNOWLEDGMENTS

The authors are grateful for fruitful discussions with Taro Nakajima, Lukas Janssen, and Matthias Vojta. The structural unit cell of the α-RuCl$_3$ was illustrated using the software `VESTA` [76]. D.G.M. acknowledges support from the Gordon and Betty Moore Foundation's EPiQS Initiative, Grant No. GBMF9069. S.N. was supported by the U.S. Department of Energy Office of Science, Basic Energy Sciences, Division of Scientific User Facilities. We acknowledge financial support from the German Research Foundation (DFG) through the Collaborative Research Center SFB 1143 (project-id 247310070), the Würzburg-Dresden Cluster of Excellence on Complexity and Topology in Quantum Matter ct.qmat (EXC 2147, project-id 390858490), and funding through DFG Project No. 411289067 (VA117/15-1) and TRR 288-422213477 (Project No. A05). V.K. was supported by the Alexander von Humboldt Foundation.

---

[1] S. Sachdev, Nat. Phys. **4**, 173 (2008).
[2] L. Balents, Nature (London) **464**, 199 (2010).
[3] M. R. Norman, Rev. Mod. Phys. **88**, 041002 (2016).
[4] J. G. Rau, E. K.-H. Lee, and H.-Y. Kee, Annu. Rev. Condens. Matter Phys. **7**, 195 (2016).
[5] S. M. Winter, A. A. Tsirlin, M. Daghofer, J. van den Brink, Y. Singh, P. Gegenwart, and R. Valentí, J. Phys.: Condens. Matter **29**, 493002 (2017).
[6] H. Takagi, T. Takayama, G. Jackeli, G. Khaliullin, and S. E. Nagler, Nat. Rev. Phys. **1**, 264 (2019).
[7] C. Broholm, R. J. Cava, S. A. Kivelson, D. G. Nocera, M. R. Norman, and T. Senthil, Science **367**, 6475 (2020).
[8] C. Nayak, S. H. Simon, A. Stern, M. Freedman, and S. Das Sarma, Rev. Mod. Phys. **80**, 1083 (2008).
[9] A. Kitaev, Ann. Phys. **321**, 2 (2006), january Special Issue.
[10] R. D. Johnson, S. C. Williams, A. A. Haghighirad, J. Singleton, V. Zapf, P. Manuel, I. I. Mazin, Y. Li, H. O. Jeschke, R. Valentí, and R. Coldea, Phys. Rev. B **92**, 235119 (2015).
[11] J. A. Sears, M. Songvilay, K. W. Plumb, J. P. Clancy, Y. Qiu, Y. Zhao, D. Parshall, and Y.-J. Kim, Phys. Rev. B **91**, 144420 (2015).
[12] J. Nasu, J. Knolle, D. L. Kovrizhin, Y. Motome, and R. Moessner, Nat. Phys. **12**, 912 (2016).
[13] S.-H. Do, S.-Y. Park, J. Yoshitake, J. Nasu, Y. Motome, Y. S. Kwon, D. T. Adroja, D. J. Voneshen, K. Kim, T.-H. Jang, J.-H. Park, K.-Y. Choi, and S. Ji, Nat. Phys. **13**, 1079 (2017).

[14] N. Janša, A. Zorko, M. Gomilšek, M. Pregelj, K. W. Krämer, D. Biner, A. Biffin, C. Rüegg, and M. Klanjšek, Nat. Phys. **14**, 786 (2018).

[15] Y. Motome and J. Nasu, J. Phys. Soc. Jpn. **89**, 012002 (2020).

[16] H. Li, D.-W. Qu, H.-K. Zhang, Y.-Z. Jia, S.-S. Gong, Y. Qi, and W. Li, Phys. Rev. Res. **2**, 043015 (2020).

[17] R. Yadav, N. A. Bogdanov, V. M. Katukuri, S. Nishimoto, J. van den Brink, and L. Hozoi, Sci. Rep. **6**, 37925 (2016).

[18] S.-H. Baek, S.-H. Do, K.-Y. Choi, Y. S. Kwon, A. U. B. Wolter, S. Nishimoto, J. van den Brink, and B. Büchner, Phys. Rev. Lett. **119**, 037201 (2017).

[19] A. Banerjee, P. Lampen-Kelley, J. Knolle, C. Balz, A. A. Aczel, B. Winn, Y. Liu, D. Pajerowski, J. Yan, C. A. Bridges, A. T. Savici, B. C. Chakoumakos, M. D. Lumsden, D. A. Tennant, R. Moessner, D. G. Mandrus, and S. E. Nagler, npj Quantum Mater. **3**, 8 (2018).

[20] L. J. Sandilands, Y. Tian, K. W. Plumb, Y.-J. Kim, and K. S. Burch, Phys. Rev. Lett. **114**, 147201 (2015).

[21] C. Balz, P. Lampen-Kelley, A. Banerjee, J. Yan, Z. Lu, X. Hu, S. M. Yadav, Y. Takano, Y. Liu, D. A. Tennant, M. D. Lumsden, D. Mandrus, and S. E. Nagler, Phys. Rev. B **100**, 060405(R) (2019).

[22] A. Sahasrabudhe, D. A. S. Kaib, S. Reschke, R. German, T. C. Koethe, J. Buhot, D. Kamenskyi, C. Hickey, P. Becker, V. Tsurkan, A. Loidl, S. H. Do, K. Y. Choi, M. Grüninger, S. M. Winter, Z. Wang, R. Valentí, and P. H. M. van Loosdrecht, Phys. Rev. B **101**, 140410(R) (2020).

[23] D. Wulferding, Y. Choi, S.-H. Do, C. H. Lee, P. Lemmens, C. Faugeras, Y. Gallais, and K.-Y. Choi, Nat. Commun. **11**, 1603 (2020).

[24] Y. Wang, G. B. Osterhoudt, Y. Tian, P. Lampen-Kelley, A. Banerjee, T. Goldstein, J. Yan, J. Knolle, H. Ji, R. J. Cava, J. Nasu, Y. Motome, S. E. Nagler, D. Mandrus, and K. S. Burch, npj Quantum Mater. **5**, 14 (2020).

[25] A. U. B. Wolter, L. T. Corredor, L. Janssen, K. Nenkov, S. Schönecker, S.-H. Do, K.-Y. Choi, R. Albrecht, J. Hunger, T. Doert, M. Vojta, and B. Büchner, Phys. Rev. B **96**, 041405(R) (2017).

[26] S. Bachus, D. A. S. Kaib, Y. Tokiwa, A. Jesche, V. Tsurkan, A. Loidl, S. M. Winter, A. A. Tsirlin, R. Valentí, and P. Gegenwart, Phys. Rev. Lett. **125**, 097203 (2020).

[27] Z. Wang, S. Reschke, D. Hüvonen, S.-H. Do, K.-Y. Choi, M. Gensch, U. Nagel, T. Rõom, and A. Loidl, Phys. Rev. Lett. **119**, 227202 (2017).

[28] C. Wellm, J. Zeisner, A. Alfonsov, A. U. B. Wolter, M. Roslova, A. Isaeva, T. Doert, M. Vojta, B. Büchner, and V. Kataev, Phys. Rev. B **98**, 184408 (2018).

[29] Y. Kasahara, K. Sugii, T. Ohnishi, M. Shimozawa, M. Yamashita, N. Kurita, H. Tanaka, J. Nasu, Y. Motome, T. Shibauchi, and Y. Matsuda, Phys. Rev. Lett. **120**, 217205 (2018).

[30] R. Hentrich, M. Roslova, A. Isaeva, T. Doert, W. Brenig, B. Büchner, and C. Hess, Phys. Rev. B **99**, 085136 (2019).

[31] R. Hentrich, A. U. B. Wolter, X. Zotos, W. Brenig, D. Nowak, A. Isaeva, T. Doert, A. Banerjee, P. Lampen-Kelley, D. G. Mandrus, S. E. Nagler, J. Sears, Y.-J. Kim, B. Büchner, and C. Hess, Phys. Rev. Lett. **120**, 117204 (2018).

[32] P. Czajka, T. Gao, M. Hirschberger, P. Lampen-Kelley, A. Banerjee, J. Yan, D. G. Mandrus, S. E. Nagler, and N. P. Ong, Nat. Phys. **17**, 915 (2021).

[33] Y. Kasahara, T. Ohnishi, Y. Mizukami, O. Tanaka, S. Ma, K. Sugii, N. Kurita, H. Tanaka, J. Nasu, Y. Motome, T. Shibauchi, and Y. Matsuda, Nature (London) **559**, 227 (2018).

[34] T. Yokoi, S. Ma, Y. Kasahara, S. Kasahara, T. Shibauchi, N. Kurita, H. Tanaka, J. Nasu, Y. Motome, C. Hickey *et al.*, Science **373**, 568 (2021).

[35] M. Yamashita, J. Gouchi, Y. Uwatoko, N. Kurita, and H. Tanaka, Phys. Rev. B **102**, 220404(R) (2020).

[36] J. A. N. Bruin, R. R. Claus, Y. Matsumoto, N. Kurita, H. Tanaka, and H. Takagi, arXiv:2104.12184 (2021).

[37] T. T. Mai, A. McCreary, P. Lampen-Kelley, N. Butch, J. R. Simpson, J.-Q. Yan, S. E. Nagler, D. Mandrus, A. R. Hight Walker, and R. V. Aguilar, Phys. Rev. B **100**, 134419 (2019).

[38] M. He, X. Wang, L. Wang, F. Hardy, T. Wolf, P. Adelmann, T. Brückel, Y. Su, and C. Meingast, J. Phys.: Condens. Matter **30**, 385702 (2018).

[39] S. Gass, P. M. Cônsoli, V. Kocsis, L. T. Corredor, P. Lampen-Kelley, D. G. Mandrus, S. E. Nagler, L. Janssen, M. Vojta, B. Büchner, and A. U. B. Wolter, Phys. Rev. B **101**, 245158 (2020).

[40] R. Schönemann, S. Imajo, F. Weickert, J. Yan, D. G. Mandrus, Y. Takano, E. L. Brosha, P. F. S. Rosa, S. E. Nagler, K. Kindo, and M. Jaime, Phys. Rev. B **102**, 214432 (2020).

[41] G. Jackeli and G. Khaliullin, Phys. Rev. Lett. **102**, 017205 (2009).

[42] S. M. Winter, Y. Li, H. O. Jeschke, and R. Valentí, Phys. Rev. B **93**, 214431 (2016).

[43] Y. Vinkler-Aviv and A. Rosch, Phys. Rev. X **8**, 031032 (2018).

[44] M. Ye, G. B. Halász, L. Savary, and L. Balents, Phys. Rev. Lett. **121**, 147201 (2018).

[45] M. Ye, L. Savary, and L. Balents, arXiv:2103.04223 (2021).

[46] I. A. Leahy, C. A. Pocs, P. E. Siegfried, D. Graf, S.-H. Do, K.-Y. Choi, B. Normand, and M. Lee, Phys. Rev. Lett. **118**, 187203 (2017).

[47] K. A. Modic, M. D. Bachmann, B. J. Ramshaw, F. Arnold, K. R. Shirer, A. Estry, J. B. Betts, N. J. Ghimire, E. D. Bauer, M. Schmidt, M. Baenitz, E. Svanidze, R. D. McDonald, A. Shekhter, and P. J. W. Moll, Nat. Commun. **9**, 3975 (2018).

[48] K. A. Modic, B. J. Ramshaw, A. Shekhter, and C. M. Varma, Phys. Rev. B **98**, 205110 (2018).

[49] K. Riedl, Y. Li, S. M. Winter, and R. Valentí, Phys. Rev. Lett. **122**, 197202 (2019).

[50] O. Tanaka, Y. Mizukami, R. Harasawa, K. Hashimoto, K. Hwang, N. Kurita, H. Tanaka, S. Fujimoto, Y. Matsuda, E.-G. Moon, and T. Shibauchi, Nat. Phys. (2022), doi: 10.1038/s41567-021-01488-6.

[51] D. A. S. Kaib, S. Biswas, K. Riedl, S. M. Winter, and R. Valentí, Phys. Rev. B **103**, L140402 (2021).

[52] A. Banerjee, J. Yan, J. Knolle, C. A. Bridges, M. B. Stone, M. D. Lumsden, D. G. Mandrus, D. A. Tennant, R. Moessner, and S. E. Nagler, Science **356**, 1055 (2017).

[53] R. Pott and R. Schefzyk, J. Phys. E **16**, 444 (1983).

[54] J. G. Rau, Eric Kin-Ho Lee, and H.-Y. Kee, Phys. Rev. Lett. **112**, 077204 (2014).

[55] S. M. Winter, K. Riedl, P. A. Maksimov, A. L. Chernyshev, A. Honecker, and R. Valentí, Nat. Commun. **8**, 1152 (2017).

[56] S. M. Winter, K. Riedl, D. Kaib, R. Coldea, and R. Valentí, Phys. Rev. Lett. **120**, 077203 (2018).

[57] J. Cookmeyer and J. E. Moore, Phys. Rev. B **98**, 060412(R) (2018).

[58] S. Bachus, D. A. S. Kaib, A. Jesche, V. Tsurkan, A. Loidl, S. M. Winter, A. A. Tsirlin, R. Valentí, and P. Gegenwart, Phys. Rev. B **103**, 054440 (2021).

[59] P. Laurell and S. Okamoto, npj Quantum Mater. **5**, 2 (2020).

[60] S.-Y. Park, S.-H. Do, K.-Y. Choi, D. Jang, T.-H. Jang, J. Schefer, C.-M. Wu, J. Gardner, J. Park, J.-H. Park *et al.*, arXiv:1609.05690 (2016).

[61] A. Glamazda, P. Lemmens, S.-H. Do, Y. S. Kwon, and K.-Y. Choi, Phys. Rev. B **95**, 174429 (2017).

[62] L. Janssen, S. Koch, and M. Vojta, Phys. Rev. B **101**, 174444 (2020).

[63] H. B. Cao, A. Banerjee, J.-Q. Yan, C. A. Bridges, M. D. Lumsden, D. G. Mandrus, D. A. Tennant, B. C. Chakoumakos, and S. E. Nagler, Phys. Rev. B **93**, 134423 (2016).

[64] J. Chaloupka and G. Khaliullin, Phys. Rev. B **94**, 064435 (2016).

[65] A. Banerjee, C. A. Bridges, J.-Q. Yan, A. A. Aczel, L. Li, M. B. Stone, G. E. Granroth, M. D. Lumsden, Y. Yiu, J. Knolle, S. Bhattacharjee, D. L. Kovrizhin, R. Moessner, D. A. Tennant, D. G. Mandrus, and S. E. Nagler, Nat. Mater. **15**, 733 (2016).

[66] L. Janssen, E. C. Andrade, and M. Vojta, Phys. Rev. B **96**, 064430 (2017).

[67] P. Lampen-Kelley, L. Janssen, E. C. Andrade, S. Rachel, J. Q. Yan, C. Balz, D. G. Mandrus, S. E. Nagler, and M. Vojta, Field-induced intermediate phase in α-RuCl$_3$: Non-coplanar order, phase diagram, and proximate spin liquid (2018), arXiv:1807.06192 [cond-mat.str-el].

[68] C. Balz, L. Janssen, P. Lampen-Kelley, A. Banerjee, Y. H. Liu, J.-Q. Yan, D. G. Mandrus, M. Vojta, and S. E. Nagler, Phys. Rev. B **103**, 174417 (2021).

[69] N. Johannsen, A. Vasiliev, A. Oosawa, H. Tanaka, and T. Lorenz, Phys. Rev. Lett. **95**, 017205 (2005).

[70] H. Suzuki, H. Liu, J. Bertinshaw, K. Ueda, H. Kim, S. Laha, D. Weber, Z. Yang, L. Wang, H. Takahashi, K. Fürsich, M. Minola, B. V. Lotsch, B. J. Kim, H. Yavas, M. Daghofer, J. Chaloupka, G. Khaliullin, H. Gretarsson, and B. Keimer, Nat. Commun. **12**, 4512 (2021).

[71] P. A. Maksimov and A. L. Chernyshev, Phys. Rev. Res. **2**, 033011 (2020).

[72] T. Biesner, S. Biswas, W. Li, Y. Saito, A. Pustogow, M. Altmeyer, A. U. B. Wolter, B. Büchner, M. Roslova, T. Doert, S. M. Winter, R. Valentí, and M. Dressel, Phys. Rev. B **97**, 220401(R) (2018).

[73] G. Bastien, G. Garbarino, R. Yadav, F. J. Martinez-Casado, R. Beltrán Rodríguez, Q. Stahl, M. Kusch, S. P. Limandri, R. Ray, P. Lampen-Kelley, D. G. Mandrus, S. E. Nagler, M. Roslova, A. Isaeva, T. Doert, L. Hozoi, A. U. B. Wolter, B. Büchner, J. Geck, and J. van den Brink, Phys. Rev. B **97**, 241108(R) (2018).

[74] T. Nakajima, Y. Tokunaga, V. Kocsis, Y. Taguchi, Y. Tokura, and T.-h. Arima, Phys. Rev. Lett. **114**, 067201 (2015).

[75] See Supplemental Material at http://link.aps.org/supplemental/10.1103/PhysRevB.105.094410 for additional field-dependent magnetostriction measurements in canted fields and additional theoretical calculations for the angular dependence of the magnetization.

[76] K. Momma and F. Izumi, J. Appl. Crystallogr. **41**, 653 (2008).